Deutscher Luft- und Raumfahrtkongress 2018
DocumentID: 480106

Systematic Investigation of a Fixed-Pitch Small-Scale Propeller Under Non-Axial Inflow Conditions

Michael Cerny, Nikolai Herzog, Jan Faust, Marco Stuhlpfarrer, Christian Breitsamter
Technical University of Munich
Chair of Aerodynamics and Fluid Mechanics
Boltzmannstr. 15, 85748 Garching, Germany

Abstract

Small-scale fixed-pitch propellers especially on multicopter configurations experience higher angles of attack than on usual aircraft configurations. In order to improve their aerodynamic efficiency, a better understanding of the occurring flow-fields under such non-axial inflow conditions is required. Therefore, an isolated small-scale propeller is operated at a range of inflow angles from zero to 180 degrees. Experimental data obtained by measurements of forces as well as a particle image velocimetry (PIV) are compared to numerical results generated by methods of different fidelity.

Keywords

Aerodynamics · Propeller · UAV · Non-axial inflow · Wind tunnel · PIV · Free wake · CFD · URANS

Nomenclature

α_{disc}	Angle of attack of the propeller disc
α_{section}	Effective angle of attack at local blade section
Γ	Circulation
ν	Kinematic viscosity
Ω	Angular velocity
ω_y	Vorticity in y-direction
ϕ	Flow angle, $\phi = \theta - \alpha_{section}$
ψ	Wake age
σ	Propeller solidity
θ	Twist angle
ξ	Non-dimensional radius
ζ	Azimuth angle
a	Axial interference factor
a'	Tangential interference factor
B	Number of blades
c	Chord length
c_{Fz}	Side force coefficient, $c_{Fz} = \frac{F_Z}{\rho n^2 D^4}$
c_T	Thrust coefficient, $c_T = \frac{T}{\rho n^2 D^4}$
D	Drag force
F	Prandtl tip loss factor
J	Propeller advance ratio, $J = \frac{u_\infty}{nD}$
L	Lift force
n	Rotational speed
Q	Propeller torque
R	Propeller radius
r	Radial position
r_c	Viscous core radius
T	Thrust
u_∞	Inflow velocity
u_{abs}	Absolute velocity magnitude
u_{ind}	Induced velocity
$u_{p,3c/4}$	Ind. vel. component at collocation point (3/4 l)
$u_{section}$	Effective inflow velocity at local blade section
$u_{x,y,z}$	Velocities in x- (axial), y- and z-direction

1 Introduction

There is a growing number of unmanned aerial vehicles (UAVs) [9, 18]. Scalable electric motors and distributed propulsion are used for innovative aerodynamic designs. While nowadays propellers for UAVs in multirotor configurations are designed mainly for static thrust or purely axial inflow conditions, they

doi: 10.25967/480106

may also experience highly yawed inflow conditions for example during the horizontal flight [2, 17]. In order to improve the aerodynamic efficiency of innovative multirotor configurations using fixed-pitch propellers, a better understanding of the occurring flow-fields under non-axial inflow conditions for propeller configurations is required [5, 12, 14, 15, 19].

Therefore, an isolated small-scale propeller of 0.46 m diameter is operated at a range of inflow angles related to the axis of the rotor disc $\alpha_{disc} = 0°$ (axial inflow) up to $\alpha_{disc} = 180°$ (reverse inflow). Three-dimensional integral forces and moments are measured in the wind tunnel A of the Chair of Aerodynamics and Fluid Mechanics of the Technical University of Munich using a six-component underfloor balance. Flow-field visualization to analyze the blade tip vortices and the wake evolution is performed by the application of stereo particle image velocimetry (PIV) for a selected case. Experimental results are compared to numerical methods of different fidelity. A Blade Element Momentum Theory (BEMT), a time-marching Free Wake Method (FWM) and unsteady Reynolds-averaged Navier-Stokes (URANS) calculations are performed. A quantitative comparison to experimental results is performed regarding the thrust coefficient and one in-plane side force coefficient.

The presented work is conducted within a research project concerning the aerodynamic optimization of hybrid propeller-rotor-concepts (HyProp) and is supported by the Siemens AG and funded by the Bavarian Research Foundation (Bayerische Forschungsstiftung).

2 Non-Axial Inflow

There can be many reasons for a propeller experiencing non-axial inflow. Especially conventional UAV multicopter configurations with propellers on a fixed vertical axis cause highly yawed inflow conditions in horizontal flight.

But also aircraft with a conventional propeller configuration can experience angles of attack of up to 10° for example in very slow forward flight (like take-off and landing), during sideslip and during a turning flight [4]. These are aspects that have been of research interest since the beginning of the aviation history [3, 6, 8].

For applications in the field of maritime vehicles these inflow conditions are very common. Nowadays, many highly maneuverable ships are equipped with so-called azimuth thrusters. These are propellers mounted on a 360°-turnable nacelle. All control forces are performed via the effective side-forces caused by the non-axial inflow [5].

A propeller is often described as a rotating wing. However, this does not pay respect to some three-dimensional propeller-specific flow effects. Especially,

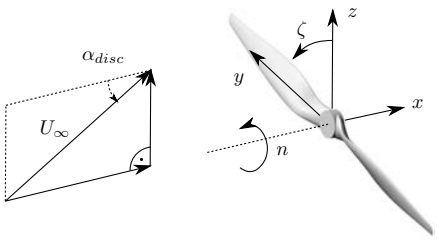

Figure 1: Definition of the applied coordinate system.

in the case of a variation of the angle of attack, the non-axial inflow leads to a highly complex three dimensional flow field (see the applied coordinate system in Fig. 1 and Fig. 2). There is a spanwise pressure gradient and a centrifugal force, accelerating in particular the separated flow radially towards the blade tip. In the rotating system of the propeller this radial velocity leads to a Coriolis force towards the trailing edge. The combination of these effects form a favorable pressure gradient, making the boundary layer more stable against static flow separation. Also, the region of separated flow is reduced which can result in an increased suction on the blades upper side [11].

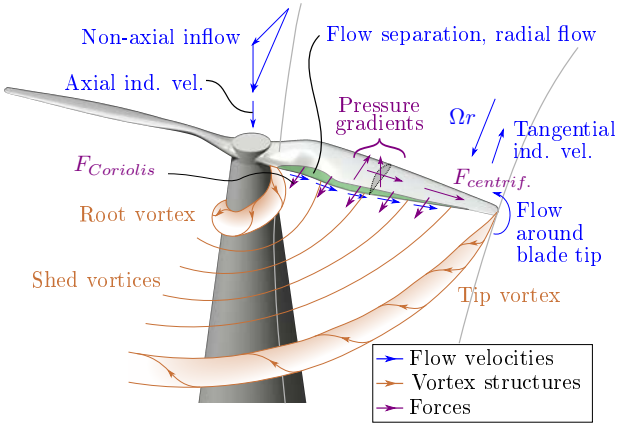

Figure 2: Flow phenomena of a propeller under non-axial inflow. Illustrated are the inflow, the rotational speed and the induced velocities, the flow around the blade tip and the radial flow. The resulting three-components pressure distribution and vortex structures are illustrated schematically.

Due to the non-axial inflow, the influence on the pressure gradients and therefore the difference between upper and lower blade side becomes periodic. Consequently, the flow separation, the radial flow and the thrust also becomes periodic. The effects on the advancing and the retreating blade are contrary, thereby pitch and yaw moments as well asymmetric tip vortices are obtained. Furthermore, within non-axial inflow there is an increased blade vortex interaction by the deflected wake causing additional time-varying loads on the propeller.

3 Experimental Approach

Within the HyProp project the small scale two-bladed fixed-pitch propeller APC 18x8E of the company APC Propellers is used. In Fig. 3 its geometrical data are illustrated.

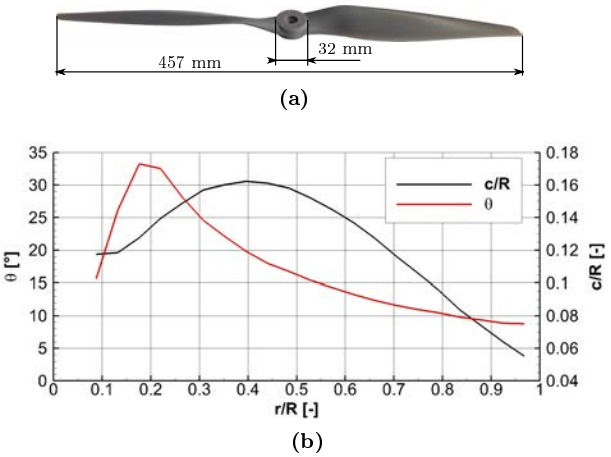

Figure 3: a. Size, b. pitch and chord length distribution of the applied APC 18x8E propeller.

The Propeller is driven by a speed controlled direct current motor (Maxon Motor EC-60-167131, electrical power 400 W). The motor is connected to a six-component underfloor balance with a resolution of 0.375 N in thrust direction and 0.75 N perpendicular to the thrust direction. The measurements are averaged over ten seconds, therefore showing the steady loads. The wind tunnel support is contained by a closed fairing, allowing for the measurement of the forces of the propeller only. The balance with the support can be rotated in the wind tunnel, enabling the measurement at inflow angles from $\alpha_{disc} = 0°$ to $\alpha_{disc} = 180°$ (see Fig. 4). Due to the long distance between the reference point of the underfloor balance and the propeller of around $l = 1.5\,\mathrm{m}$ the propeller moments are in the order of the error of the measurements. Hence, the determination of the propeller efficiency is not accurate. For this reason, only the force measurements are presented in this work.

Besides the load analyses, the flow field around the propeller is measured using stereo particle image velocimetry (PIV) at a selected inflow condition of $\alpha_{disc} = 60°$ and $J = 0.164$. To measure both the axial and the non-axial velocity components, the plane of measurement is oriented horizontally in the wind tunnel (see Fig. 5). The laser is positioned on the side of the wind tunnel on a traverse system. Both cameras are mounted above the test section on a traverse system. They are moved uniformly with the laser for different measurement positions.

For analyzing the wake, the PIV images are recorded phase locked; triggered by the motor control unit. In order to minimize the shading of the laser beam by the propeller blade, the measurements are performed with the propeller blades vertically oriented. The spatial resolution of the PIV images is around 1.5 mm. Every image covers a size of 80x80 mm. Between 40 and 70 images are merged to visualize the desired wake portion. 200 samples are taken for every position. With these data the normalized mean velocity components $\frac{\bar{u}_i}{u_\infty}$ are calculated. To define the degree of unsteadiness in the wake, the normalized RMS value of the absolute velocity magnitude is calculated by

$$\frac{u_{abs,RMS}}{u_\infty} = \frac{\sqrt{\frac{1}{N}\sum_{n=1}^{N}\left(|\boldsymbol{u}_n(t)| - |\overline{\boldsymbol{u}}|\right)^2}}{u_\infty} \qquad (1)$$

with $\overline{\boldsymbol{u}}$ being the mean velocity and $\boldsymbol{u}_n(t)$ referring to the velocity of the current sample. N denotes the number of samples.

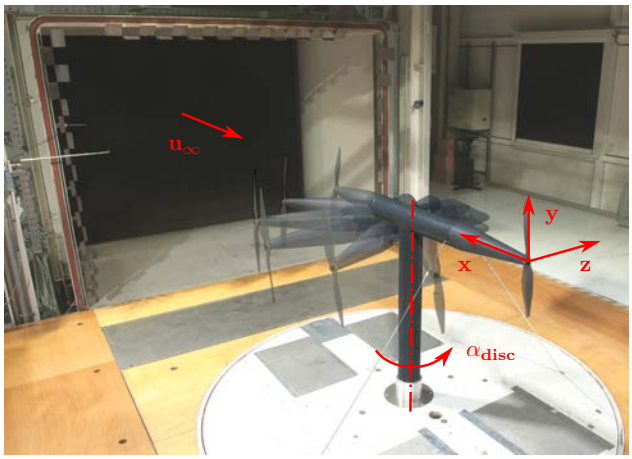

Figure 4: Rotatable wind tunnel support with mounted propeller.

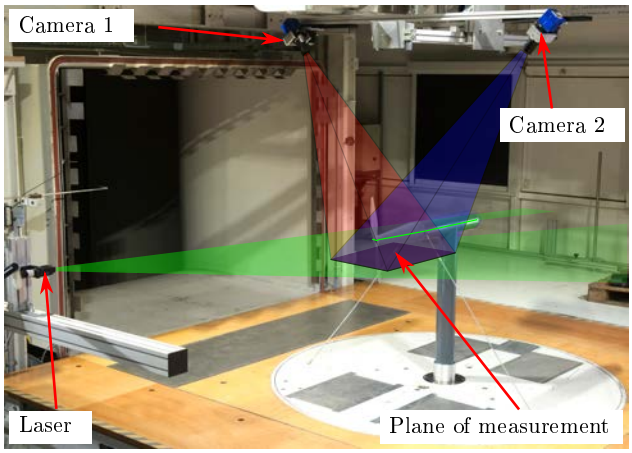

Figure 5: Stereo-PIV setup. The laser as well as the cameras are mounted on uniformly moving traverse systems. The laser illuminates the horizontally aligned plane of measurement.

4 Numerical Approach

Within this work, BEMT, FWM and URANS calculations are used to determine the aerodynamic forces onto the propeller, which are compared to the wind tunnel data. Furthermore, flow field information are calculated for comparison to PIV results. The most relevant equations to all three numerical methods are described briefly.

4.1 Blade Element Momentum Theory

The BEMT in its original form [4] represents a steady approach for the design and analysis of propellers under axial inflow. In this work, its formulation in [1] is implemented and extended to model the non-axial inflow. Therefore, the actual local inflow conditions at each azimuthal position are taken into account. The resulting velocities on a blade section are shown in Fig. 6.

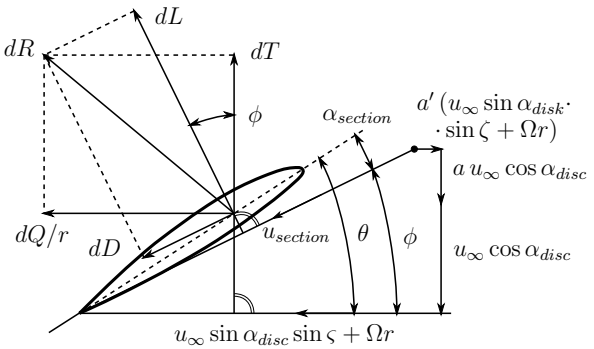

Figure 6: Inflow characteristics of a propeller's blade section under non-axial inflow. The non-axial inflow influences the local lift dL and drag dD and, furthermore, the local thrust dT and portion of propeller torque dQ/r.

The governing non-linear equations of the BEMT read for a blade element

$$\frac{a}{1+a} = \frac{\sigma c_y}{4F \sin^2\phi} \tag{2}$$

$$\frac{a'}{1-a'} = \frac{\sigma c_x}{4F \cos\phi \sin\phi} \tag{3}$$

$$\phi = \arctan \frac{u_\infty \cos\alpha_{disk} \ (1+a)}{(u_\infty \sin\alpha_{disk} \sin\zeta + \Omega r) \ (1-a')} \tag{4}$$

with

$$c_x = c_L \sin\phi + c_D \cos\phi \tag{5}$$

$$c_y = c_L \cos\phi - c_D \sin\phi \tag{6}$$

$$F = \frac{2}{\pi} \arccos\left[\exp\left(-\frac{B\,(1-\xi)}{2\,\xi \sin\phi}\right)\right] \tag{7}$$

where a, a' and ϕ represent the axial interference factor, the tangential interference factor and the flow angle. The quantities are determined for each non-dimensional radius $\xi = r/R$ and azimuthal angle ζ. B represents the number of blades, $c(r)$ the chord length at a specific section of the propeller blade, $\sigma = \frac{Bc}{2\pi\xi R}$ the sectional solidity ratio, u_∞ the inflow velocity, c_x and c_y the sectional force coefficients according to two-dimensional airfoil polar data. The losses by the flow around the blade tips are modelled by the Prandtl tip loss factor F.

The system is solved for ϕ by inserting Eq. 2 and Eq. 3 into Eq. 4 and applying a Newton method. Knowing the flow angle ϕ and the interference factors a and a' for all radial and azimuthal positions, the differential thrust coefficient can be determined by

$$\frac{\partial c_T(\xi,\,\zeta)}{\partial \xi} = \frac{c\,c_y}{4n^2D^3} \frac{u_\infty^2 \cos^2\alpha_{disc}(1+a)^2}{\sin^2\phi} \tag{8}$$

where D is the propeller diameter and n the rotational speed. For axial inflow, and thus no azimuthal dependency, all radial elements given by $\frac{\partial c_T(\xi,\zeta)}{\partial \xi}$ are to be integrated over ξ from hub to tip and multiplied by the number of blades to provide the total c_T of the propeller. At non-axial inflow, $\frac{\partial c_T(\xi,\zeta)}{\partial \xi}$ depends on the azimuthal position ζ. Integration over ξ leads to $c_T(\zeta)$ as sectoral values. In a second step, all blades are tracked over one revolution simultaneously. The values of each sector are summed up to obtain the once-per-revolution (1P) propeller load curve. Subsequently, minimum, maximum and mean values can be determined. Also, the torque coefficient and all other in-plane force and moment coefficients can be established in the same way. The spatial discretization is realized by 14 radial and 12 azimuthal elements.

Derivation of 2D Airfoil Data

The implemented BEMT and also the FWM use sectional lift and drag coefficients. These are calculated a priori using the viscid formulation within XFoil over a range of angles of attack and Reynolds numbers. An early triggered transition is set, since turbulent flow is assumed on the blades. In order to provide data for $\alpha_{section}$ in the non-linear part of the polar, the XFoil data are extrapolated with a transition onto an experimentally obtained polar, given in [16]. An exemplary sectional aerodynamic data extension is shown in Fig. 7. There is a dominant three-dimensional character within the blade's boundary layer, especially at angles of attack above the linear regime. Optionally, empirically obtained stall delay factors can be applied [11]. For simplicity these are not applied in this work.

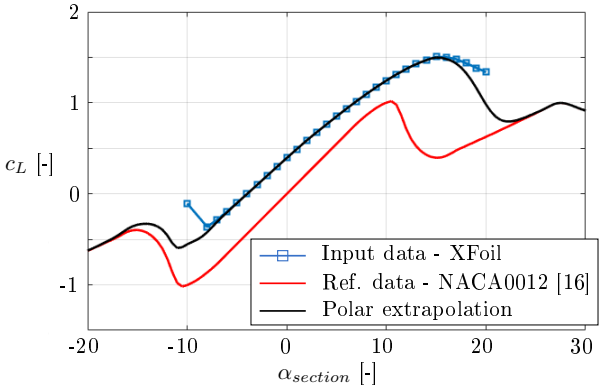

Figure 7: Sectional aerodynamic data. XFoil results at the $\xi = 0.8$ radial section for $Re = 5 \cdot 10^5$. Also shown is the extrapolation with a transition onto an experimentally obtained polar of a NACA0012 airfoil.

4.2 Free Wake Method

A method, utilizing a Lifting-Line theory coupled to a Free Wake Scheme is implemented to extend the modeling capabilities of a deflected wake under non-axial inflow.

Physical Modeling

The fundamental idea behind such concepts is to model the propeller and its wake with vortex elements. These are discretized as a vortex lattice, where the evolution of the wake is obtained through the mutual interactions of the vortex elements over time. The solution methodology is based on the separation into two problems. The inner wing problem is associated with determining the bound circulation strength of each blade section, whilst the outer wake problem governs the advection of vortex elements. The independent solutions are coupled through the induced velocity calculation at the blade collocation points. The governing equation of the second-order numerical Lifting-Line implementation given in [7] reads

$$\frac{\Gamma}{\pi c} = \frac{u_\infty}{2\pi} c_\mathrm{L} \left(\phi - \frac{u_{\mathrm{p,3c/4}}(\Gamma)}{u_\infty} \right) \tag{9}$$

with the bound circulation Γ, the sectional lift coefficient c_L, sectional chord c, free stream velocity u_∞ and $u_{\mathrm{p,3c/4}}$ being the induced velocity component at the three-quarter chord collocation point. In contrast to the BEMT, the inflow velocities at the airscrew plane are determined by a vortex wake model. The flow field solution for vortex based methods requires solving the vorticity transport equation in a time marching manner. The vorticity transport equation in blade fixed coordinates in partial differential form is expressed as

$$\frac{\partial \vec{r}(\psi,\zeta)}{\partial \psi} + \frac{\partial \vec{r}(\psi,\zeta)}{\partial \zeta} = \frac{1}{\Omega} \left[\vec{u}_\infty + \vec{u}_\mathrm{ind} \left(\vec{r}(\psi,\zeta) \right) \right] \tag{10}$$

which describes the location of each fluid marker in terms of the respective wake age ψ and current azimuth angle ζ. The difficulty arises from the strong non-linear nature of the induced velocity field $\vec{u}_\mathrm{ind}\left(\vec{r}(\psi,\zeta)\right)$. To evaluate the velocity vector at each fluid marker located at a position $\vec{r}$, the induced velocities of each discrete vortex element in the wake are computed. The induced velocities are obtained by numerical integration of the Biot-Savart law, reading

$$\vec{u}_\mathrm{ind} = \frac{\Gamma}{4\pi} \int \frac{d\vec{l} \times \vec{r}}{|\vec{r}|^3} \tag{11}$$

where Γ is the circulation strength of each discrete vortex element of length $d\vec{l}$. To avoid the singularity as $|\vec{r}|$ approaches zero, a cut-off distance in terms of a viscous core radius r_c is used. It is set to a value of 5 % of the blade chord at the tip, which corresponds to the airfoil thickness at the blade tip where the vortex is created [13].

Discretization and Numerical Integration

For a more efficient computation, the wake is further discretized by a near wake part with a vortex lattice and a far wake in form of one tip and one root vortex. The near wake length is set to 90 degrees. It models the trailed and shed vorticity near the blades. The total vorticity of the near wake is transferred into the root and the tip vortices of the far wake.

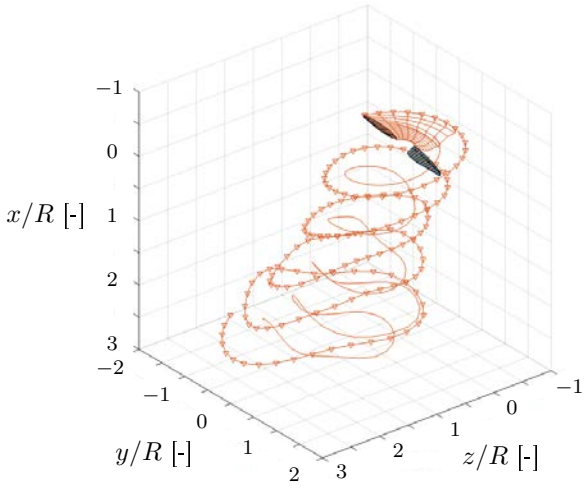

Figure 8: Discretization for FWM. Vortex elements of the near wake and the far wake are shown.

For the spatial discretization 14 radial elements are used to resolve each blade, and for the temporal discretization 12° increments in azimuth are applied. In Fig. 8, an impression of the discretization can be seen. The near wake lattice and the tip and root vortices of the far wake are shown for one blade with the corresponding discretization. The numerical integration is accomplished by using a predictor-corrector second order backward (PC2B) scheme [10].

4.3 URANS Calculations

Using a finite volume method, the incompressible URANS equations for mass and momentum are solved on an unstructured grid. The commercial software Simcenter Star-CCM+ is used which enables an automated meshing and all pre- and and postprocessing tasks within its environment. An overview of the mesh dimensions and the numerical settings is given in the following.

Computational Mesh

The computational mesh is created within a static hexahedral geometry with a cylindrical domain in the center containing the propeller geometry. The cylindrical domain including the propeller rotates with the rotational speed. The flow solution is obtained by the sliding mesh technique. On both parts of the interface, prism layers of equal cell size are generated to improve the numerical accuracy. The mesh consists of polyhedral cells to reduce the number of tetrahedral cells by the factor of five. Towards all body surfaces, structured prism layers are created to resolve the boundary layer. Especially at the blades, 25 prism layers are used. The transition of adjacent cell sizes within the polymesh is less than a volume factor of 0.8. The prism layer cells are continuously removed if the expansion growth condition is not satisfied. An impression of the domain near the propeller and the resolution at a representative blade section at the $\xi = 0.75$ radial section can be seen in Fig. 9b. In the CFD simulation a dimensionless wall distance of $y^+ \approx 1.3$ is achieved in order to accurately resolve the viscous sublayer. The number of cells in the static domain is about 5 million and the rotating part contains about 10 million cells.

Physical Modeling

The numerical calculations are performed using a pressure-based segregated solver. The blade tip Mach number is at maximum about $M_{tip} \approx 0.28$. Hence, density and temperature changes are not modeled in order to reduce the computational effort. The timestep is set to move the rotating domain one degree per time-step. The spatial and temporal gradients are discretized with a second order scheme. The used solver is based on the SIMPLE algorithm. Aside from the outlet, where a pressure outlet is used, the velocity inlet boundary with the respective inflow velocity vector is applied. For all calculations, the $k - w$ shear stress transport (SST) turbulence model using the standard settings is applied. The simulation is conducted over nine propeller revolutions leading to a computational time of 232 hours on 39 CPUs.

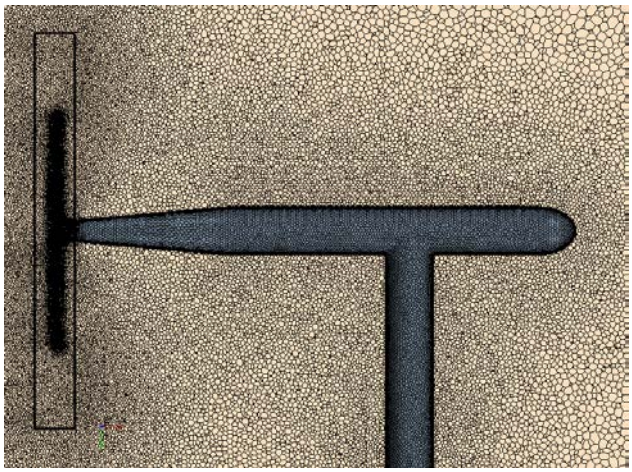

(a)

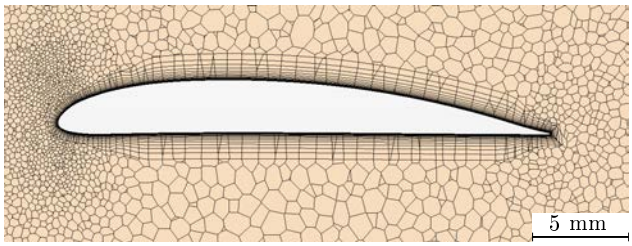

(b)

Figure 9: Mesh section views. (a) Zoom into the domain mid-section showing the rotating part around the propeller and the geometry of the wind tunnel support. (b) Mesh of propeller airfoil section at the $\xi = 0.75$ radial section.

5 Results and Discussion

At first, the results for the thrust coefficient and the side force coefficient in z-direction c_{Fz} (see the coordinate system in Fig. 1) are discussed. The second part contains the flow field discussion of the PIV and the URANS results.

Load Polar

For both force coefficients c_T and c_{Fz}, two load polars are generated at a constant rotational speed of $n = 4000\,\mathrm{min}^{-1}$ and two freestream velocities $u_\infty = \{5m/s, 15m/s\}$. This represents the axial advance ratios of $J = \{0.164, 0.492\}$. For axial inflow conditions, disc loadings of about $DL = 100\,\mathrm{N/m^2}$and $DL = 25\,\mathrm{N/m^2}$ are obtained. The results of the BEMT and the FWM are compared to the wind tunnel results in Fig. 10 and Fig. 11 (BEMT for $\alpha_{disc} \leq 90°$). In general, the cosine trend of both polars is captured. The force coefficients correlated to the two inflow conditions are met with different accuracy, as described in the following.

Looking first at the thrust coefficient results for the lower advance ratio $J = 0.164$, the trend of increasing thrust is predicted well with the FWM and the BEMT up to $\alpha_{disc} = 70°$.

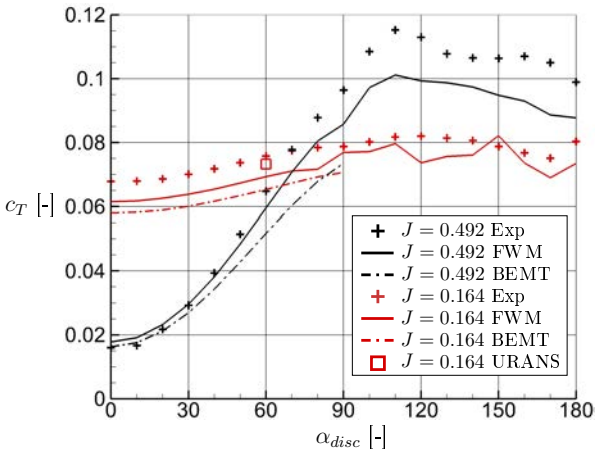

Figure 10: Thrust coefficient c_T over the inflow angle α_{disc} for $u_\infty = \{5m/s, 15m/s\}$.

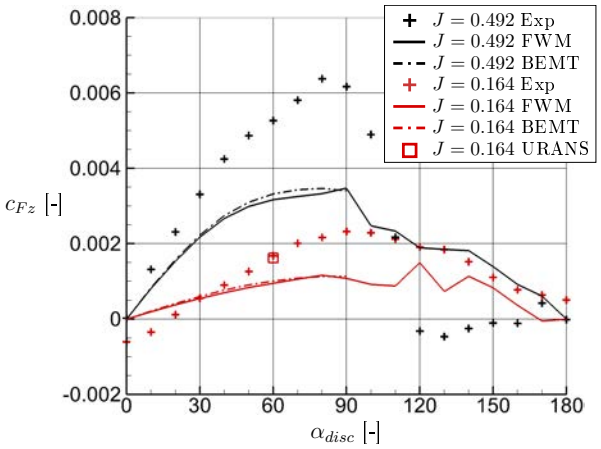

Figure 11: Side force coefficient c_{Fz} over the inflow angle α_{disc} for $u_\infty = \{5m/s, 15m/s\}$.

Here, the FWM results are constantly 10 % below and the BEMT results 17 % below the experimental results. For $\alpha_{disc} > 70°$, the FWM results show an oscillatory behavior due to the positions of the vortex elements within the strongly deflected wake.

Considering the results for the high advance ratio, only the trend is captured well. From axial inflow to $\alpha_{disc} = 20°$ the FWM and the BEMT results are 10 % respectively 2 % higher than the experimental results. The slope for an increasing α_{disc} is below the experimental results for both methods. The experimental polar intersects the calculated polar by BEMT at about $\alpha_{disc} \approx 20°$ while FWM polar intersects at about $\alpha_{disc} \approx 30°$. Beyond these inflow angles, the slopes of the experimental and both numerical results diverge. At $\alpha_{disc} = 90°$ the FWM and the BEMT results are 10 % respectively 20 % below the experimental results. In general, both the experimental data as well as the FWM results show a peak value at $\alpha_{disc} = 110°$. Also, the decrease of c_T for inflow angles $\alpha_{disc} > 110°$ at the higher advance ratio is captured by the FWM.

Besides the BEMT and the FWM results, one representative URANS result at $\alpha_{disc} = 60°$ and $J = 0.164$ is shown. This URANS calculation shows the best agreement with the experimental results. The flow field for this inflow condition is discussed in the next section in detail.

The results for the side fore coefficient c_{Fz} are shown in figure 11. The higher advance ratio shows a higher side-force in z-direction. While the peak of the experimental results is at $\alpha_{disc} = 80°$ for $J = 0.492$, it is at $\alpha_{disc} = 90°$ for $J = 0.164$. Looking at the experimental results for $J = 0.164$, an offset can be detected. This can be attributed to the precision of the underfloor balance and the measurement procedure, where the aerodynamic loads are obtained by subtracting the loads of the wind tunnel support from the total loads.

Nonetheless, the deviation is constant within a polar, enabling the evaluation of the trends. The measured values are underestimated by the BEMT and the FWM for both advance ratios. The peaks are captured by the BEMT, while the FWM polar shows again an oscillatory behavior for $\alpha_{disc} \geq 80°$.

Flow Field

The PIV data are used to visualize the flow in the cross-section of the propeller wake. The measurements are performed at an inflow angle of $\alpha_{disc} = 60°$, an advance ratio of $J = 0.1635$ and a disc loading of $DL = 109.7\,\mathrm{N/m^2}$. In Fig. 12, the resulting velocity in x-direction (propeller rotational axis) is shown, normalized with the inflow velocity u_∞. The white areas within the flow field are blanked due to reflections of the propeller and the support structure. One can see the acceleration of the fluid as well as the corresponding contraction of the wake. The limiting streamline of the propeller shows a curved behavior: Close to the propeller the wake almost follows the rotational axis. Further downstream it tends to align towards the inflow direction. In the center of the wake, a region of low axial velocity is located. This correlates to the hub and the inner part of the blades. Flow separation occurs and a root vortex (RV) is formed. For comparison, in Fig. 14 the same flow conditions are modeled with the URANS calculation. In comparison to the experimental data, the velocity in the center of the wake is overpredicted. Additionally, the traces of the two tip vortices as calculated with the FWM can bee seen in Fig. 12. One can see that for the region of the first two rotations the positions of the tip vortices are predicted in good agreement with the experiment, although the support is modeled in the FWM.

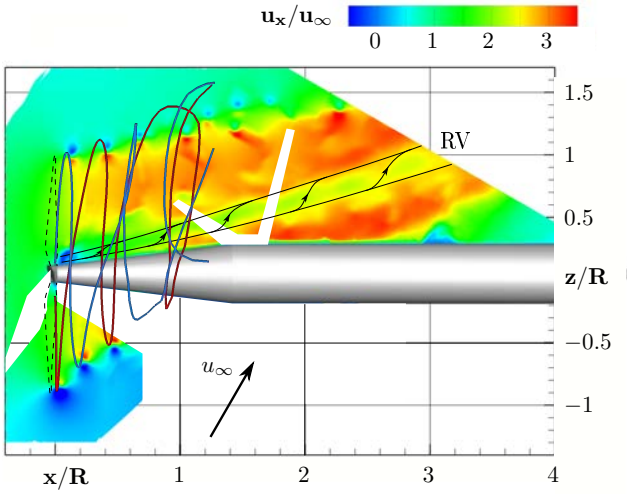

Figure 12: Normalized axial velocity component u_x/u_∞ and the blade tip vortices of the FWM. PIV measurement, $J = 0.164$, $\alpha_{disc} = 60°$.

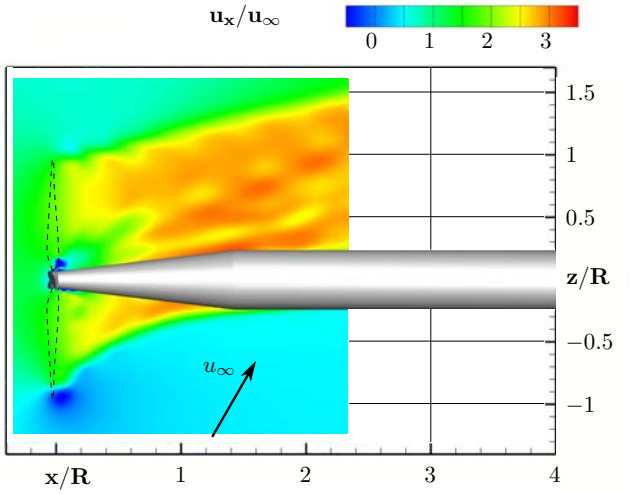

Figure 14: Normalized axial velocity component u_x/u_∞. In comparison to the experimental data, the velocity in the center of the wake is overestimated. Derived from URANS data, $J = 0.164$, $\alpha_{disc} = 60°$.

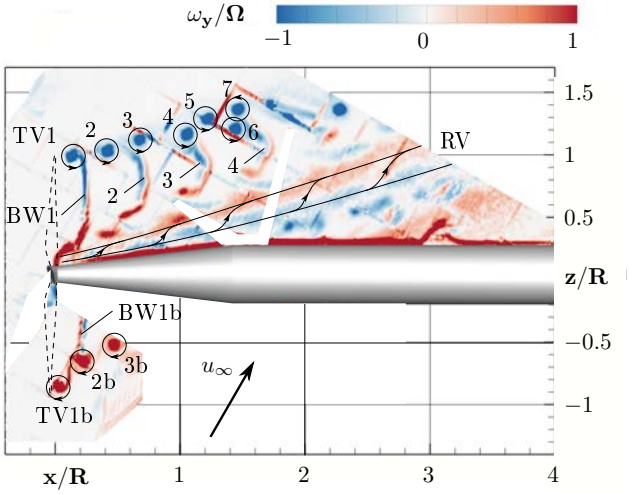

Figure 13: Normalized vorticity component in y-direction ω_y/Ω. Both the strong tip vortices (TV) as well as the blade wakes (BW) can be seen. The tip vortices have a mutual influence causing a deflection in the positive or the negative z-direction. PIV measurement, $J = 0.164$, $\alpha_{disc} = 60°$.

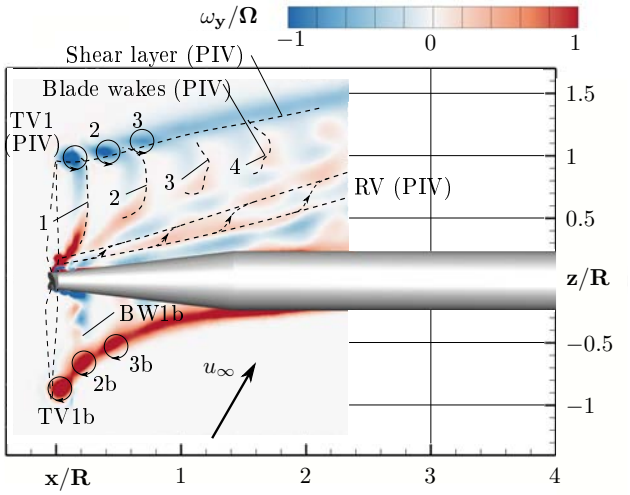

Figure 15: Normalized vorticity component in y-direction ω_y/Ω. Derived from URANS data, $J = 0.164$, $\alpha_{disc} = 60°$. The dashed curves are the PIV results.

Further downstream, the missing dissipation modeling in the FWM causes non-physical structures in its wake. Therefore, the vortex traces are blanked for $x/R > 1.3$.

The illustration of the vorticity component in y-direction (see Fig. 13 and coordinate system in Fig. 1) provides a deeper understanding of the flow field. The flow around the blade tips forms the strong tip vortices (TV) which can be seen on both the luv and the lee side of the support. Also, their behavior when convecting downstream can be seen.

Their mutual influence induces a deflection in the positive or the negative z-direction. Obviously, the wakes of the individual propeller blades (BW) can be seen on the leeward side of the support structure and their convection downstream as shed vortices. Also the deformation of these wakes can be seen. The root vortex (RV) itself is barely visible since its vorticity is oriented mainly in the x-direction. However, one can see the shear layer around the vortex, caused by the velocity difference between the slow wake core and the accelerated outer region.

The results of the URANS simulation (see Fig. 15) show a good agreement with the experiment, especially the positions of the first tip vortices and the evolution

of the blade wakes. Also it can be seen, that, when compared to the trace of the outer shear layer of the PIV results, the deflection of the wake is in good agreement. However, the downstream convection of the tip vortices and the blade wakes is underestimated. Furthermore, the tip vortices do not interact with each other (the deflection is missing). They are less focused and dissipate further upstream. The root vortex is less stable compared to the PIV results. One reason for this is the overprediction of the velocity in the core region of the wake. Since there is no velocity gradient, no isolating shear layer between the core and the outer region of the wake is formed.

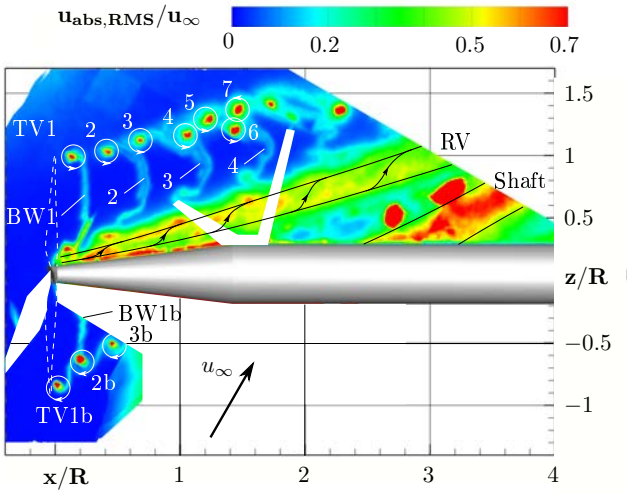

Figure 16: Normalized RMS value of the velocity magnitude $u_{abs,RMS}/u_\infty$. PIV measurement, $J = 0.164$, $\alpha_{disc} = 60°$.

In order to measure the unsteadiness of the wake, the normalized RMS values of the velocity magnitudes are calculated (see Eq. 1) and shown in Fig. 16. Close to the propeller plane, the tip vortices are visible as focused points. Hence, the vortices are stationary in the region. Further downstream the tip vortices are less stationary due to the mutual influence and the consequent deflection of the vortices. In contrary, the trace of the blade wakes and their evolution can be considered as stationary. The flow region of the root vortex appears to be very unsteady. An explanation is the interaction of two occurring flow structures, namely the root vortex and the shear layer between the core and the outer wake region. Both are related to a strong radial velocity gradient between the wake core and the outer region. Another region of high RMS values can be seen further downstream at around $x/R \approx 3$. This region is the lee side of the vertical shaft of the support structure which causes strong turbulence in the flow field.

6 Conclusion and Outlook

The influence of a non-axial inflow on a small scale propeller was analyzed by force measurements at different inflow angles and advance ratios. In addition, investigations of the flow field for a selected inflow condition were performed by the application of PIV. Three different numerical approaches were conducted to predict the thrust and the side force coefficient as well as the flow field character.

The experimental force measurements showed the influence of the angle between the propeller disc and the inflow velocity vector on the thrust and the side force coefficient. The numerical results of the BEMT and the FWM showed, that the methods are capable to predict the trend of the coefficients up to $\alpha_{disc} = 90°$ respectively to $\alpha_{disc} = 180°$. The deviation to the experimental results is below 20 % for the thrust but up to 40 % larger for the side force. An exemplary result by unsteady Reynolds-averaged Navier-Stokes calculations showed the closest agreement with the experiment.

Performing the PIV measurements, an impression of the wake in the propeller's cross-section at an inflow angle of $\alpha_{disc} = 60°$ was obtained. Wake characteristics like tip and root vortices and the blade wake convection and evolution are captured. Close to the propeller plane, the positions of the tip vortices and the blade wakes out of the URANS calculation are in good agreement with the PIV measurement. The mixing of the wake when flowing around the wind tunnel support structure is also comparable between the PIV and the URANS results. The velocity of the core of the wake is overpredicted in the URANS result. Additionally, also the FWM was capable of predicting the positions of the tip vortices quantitatively correct for the first three propeller rotations.

Future work represents the usage of an internal model-integrated balance, having a higher accuracy and enabling the measurement of moments and with a temporal resolution in order to compare once per revolution load curves. Furthermore, the flow field at higher inflow angles will be analyzed.

7 Acknowledgements

The authors would like to thank the Bavarian Research Foundation (Bayerische Forschungsstiftung) for the funding of the HyProp research project. Further, the successful collaboration and support by the project partner Siemens AG is highly acknowledged. Special thanks are addressed to Siemens Star-CCM+ for providing the flow simulation software. Last but not least, the authors thank the company APC Propellers for providing the geometrical data of the analyzed propeller.

Literature

[1] Charles N. Adkins and Robert H. Liebeck. Design of Optimum Propellers. *Journal of Propulsion and Power*, 10(5):676–682, 1994.

[2] Pierre-Jean Bristeau, Philippe Martin, Erwan Salaün, and Nicolas Petit. The Role of Propeller Aerodynamics in the Model of a Quadrotor UAV. In *European Control Conference, Aug. 23-26, 2009*, pages 683–688, Budapest, Hungary.

[3] Hermann Glauert. The Stability Derivatives of an Airscrew. *Reports and Memoranda, British A. C. A*, (No. 642), 1919.

[4] Hermann Glauert. *Aerodynamic Theory - Division L - Airplane Propellers.* Julius Springer (Berlin), Farnborough, England, 1935.

[5] Amini Hamid and Steen Sverre. Experimental and Theoretical Analysis of Propeller Shaft Loads in Oblique Inflow. *Journal of Ship Research*, 55(4):1–21, 2011.

[6] R. G. Harris. Forces on a Propeller Due to Sideslip. *Reports and Memoranda, British A. C. A*, (No. 427), 1918.

[7] Wayne Johnson. *CAMRAD II - Comprehensive Analytical Model of Rotorcraft Aerodynamics and Dynamics - Volume I : Theory.* Johnson Aeronautics, Palo Alto, California, 2017.

[8] Frederick W. Lanchester. *The Flying-Machine from an Engineering Standpoint.* Constable & Co., Ltd., London, 1917.

[9] Miriam Leis. Drones in Logistics. In *Danish-German Drone R&D Workshop, March 31st, 2017*, Munich, Germany. Fraunhofer Think Tank.

[10] J. Gordon Leishman. *Principles of Helicopter Aerodynamics.* Cambridge Univeristy Press, Cambridge, 2nd edition, 2006.

[11] C. Lindenburg. Modelling of Rotational Augmentation Based on Engineering Considerations and Measurements. *European Wind Energy Conference, London, Nov. 22-25, 2004.*

[12] Jason L. Pereira. *Hover and Wind-Tunnel Testing of Shrouded Rotors for Improved Micro Air Vehicle Design.* PhD thesis, University of Maryland, College Park, 2008.

[13] Manikandan Ramasamy and J. Gordon Leishman. Interdependence of Diffusion and Straining of Helicopter Blade Tip Vortices. *Journal of Aircraft*, 41(5):1014–1024, 2004.

[14] Carl R. Russell and Martin K. Sekula. Comprehensive analysis modeling of small-scale UAS rotors. In *AHS International 73rd Annual Forum & Technology Display, May 9-11, 2017*, Fort Worth, Texas, USA, 2017.

[15] Carl R Russell, Colin R Theodore, Moffett Field, Martin K Sekula, and Aeroelasticity Branch. Incorporating Test Data for Small UAS at the Conceptual Design Level. In *AHS International Technical Conference on Aeromechanics Design for Transformative Vertical Flight, San Francisco, CA, January 16-18, 2018*, 2018.

[16] R. E. Sheldahl and P. C. Klimas. *Aerodynamic Characteristics of Seven Symmetrical Airfoil Sections through 180-Degree Angle of Attack for Use in Aerodynamic Analysis of Vertical Axis Wind Turbines.* Sandia National Labs, Albuquerque, New Mexico, USA, 1981.

[17] B. Theys, G. Dimitriadis, T. Andrianne, P. Hendrick, and J. De Schutter. Wind Tunnel Testing of a VTOL MAV Propeller in Tilted Operating Mode. In *International Conference on Unmanned Aircraft Systems (ICUAS), May 27-30, 2014*, pages 1064–1072, Orlando, Florida.

[18] Visiongain. Small Unmanned Aerial Vehicle (UAV) Market Forecast 2015-2025: Micro, Mini, Nano UAVs in Military, Homeland Security, Law Enforcement, Industrial, Media, Agriculture & Scientific Applications. 2015.

[19] Wenwu Zhou, Zhe Ning, Haixing Li, and Hui Hu. An Experimental Investigation on Rotor-to-Rotor Interactions of Small UAV Propellers. In *35th AIAA Applied Aerodynamics Conference, June 5-9, 2017*, Denver, Colorado, USA.